Article

Statistical Deviations in Shoreline Detection Obtained with Direct and Remote Observations

Giovanni Pugliano [1] , **Umberto Robustelli** [1,*] , **Diana Di Luccio** [2,*] , **Luigi Mucerino** [3] , **Guido Benassai** [1] **and Raffaele Montella** [2]

1   Science and Technologies Department, University of Naples "Parthenope", 80143 Napoli, Italy;
    giovanni.pugliano@uniparthenope.it (G.P.); guido.benassai@uniparthenope.it (G.B.)
2   Engineering Department, University of Naples "Parthenope", 80143 Napoli, Italy;
    raffaele.montella@uniparthenope.it
3   Department of Earth, Environment and Life Sciences, University of Genova, 16126 Genova, Italy;
    luigi.mucerino@edu.unige.it
*   Correspondence: umberto.robustelli@uniparthenope.it (U.R.); diana.diluccio@uniparthenope.it (D.D.L.)

Abstract: Remote video imagery is widely used for shoreline detection, which plays a fundamental role in geomorphological studies and in risk assessment, but, up to now, few measurements of accuracy have been undertaken. In this paper, the comparison of video-based and GPS-derived shoreline measurements was performed on a sandy micro-tidal beach located in Italy (central Tyrrhenian Sea). The GPS survey was performed using a single frequency, code, and carrier phase receiver as a rover. Raw measurements have been post-processed by using a carrier-based positioning algorithm. The comparison between video camera and DGPS coastline has been carried out on the whole beach, measuring the error as the deviation from the DGPS line computed along the normal to the DGPS itself. The deviations between the two dataset were examined in order to establish possible spatial dependence on video camera point of view and on beach slope in the intertidal zone. The results revealed that, generally, the error increased with the distance from the acquisition system and with the wash up length (inversely proportional to the beach slope).

Keywords: DGPS measurements; video camera observation; shoreline position; beach survey

1. Introduction

Coastal areas are highly dynamic environments that provide important benefits, but are also subject to a variety of natural hazards such as beach erosion, tsunamis [1,2], and floods [3]. For coastal zone monitoring and coastal risk assessment [4], shoreline detection is a fundamental work. The shoreline is the line where land meets the sea, and due to the dynamic nature of the sea, sometimes it is difficult to determine a precise line that can be called the "shoreline". As reported by Boak and Turner [5], a functional definition of the "shoreline", which has to consider the shoreline in both a temporal and spatial sense, is required.

Many authors highlighted the existence of different methodologies for coastal monitoring [6–9], not only limited to shoreline detection, based on direct and remote acquisition systems.

Direct shoreline surveys are normally carried out using the GPS technique by post-processing or real-time methods [10]. The main limitation of this method is the huge time required for covering large stretches of the coastline and the difficulties inherent in doing ad hoc timely post-storm measurements.

Remote shoreline observations can be distinguished in remote sensing [11–13], UAV (Unmanned Aerial Vehicles) [14], and video monitoring [15,16], which were first introduced by Aarninkhof [17] and Turner et al. [18]. These remote observations have been also extensively used to validate wind

and wave numerical models [19–23] and to outline the environmental big picture in marine spatial planning applications [24–26].

In addition to using UAVs in beach survey [27,28], video monitoring can provide a remotely-sensed measurement, fixed at a secure location (e.g., a tower or high-point), with the capability of acquiring imagery at a frequency ranging from fractions of seconds to hours. The technology is relatively low-cost, but the main issue is the processing method, especially the image rectification process, considering that the imagery is strongly oblique and relies on a number of GCPs (Ground Control Points) for finding the best geometry solutions. This technique has been successfully applied for both shoreline monitoring [29,30], rip current measurement [14] and morphodynamics classification of sandy beach [31,32].

Several techniques are proposed to extract shoreline from images, based on discriminating sea from sand. Plant and Holman [33] used a method initially developed for gray-scale cameras, called Shoreline Intensity Maximum (SLIM), which defines the shoreline as the cross-shore position at which wave breaking is maximized and consequently corresponds to a maximum in pixel intensity. With the adoption of color cameras, spectral information could also be used to identify the shoreline, making use of the water property to absorb the Red signal (R) and the sand property to absorb the Green (G) and blue signal [34,35]. Following Almar et al. [36], we identify beach pixels as channel values with a high R/G ratio, whereas water pixels as high G channel values. The shoreline represents the transition zone between the two peaks. In order to smooth out high-frequency signals that are caused by disturbances like foam, we used time-exposure images [17,18].

In this paper, we performed shoreline detection by means of remote video camera observations and DGPS direct shoreline measurements on a sandy microtidal beach located in central Tyrrhenian Sea. Almar et al. [36], among other authors, have presented video-based methods to determine shoreline position in different tidal and wave energy contexts, showing an error dependence on local swash length, which is inversely proportional to the beach slope. Following this research item, we first performed a preliminary analysis of the GPS survey, which was followed by the evaluation of the statistical deviations of the video camera coastline measurements from the DGPS ones. The errors have been spatially processed, in order to examine if systematic deviations can be ascribed only to the intertidal beach slope or to additional factors, like the distance from the video camera. In particular, we examined the longitudinal and cross-shore errors associated with the video camera point of view.

The paper is structured as follows: after a brief description of the study area (Section 2), we illustrate the survey and validation methods used in Section 3. The results with the relative discussion are reported in Sections 5 and 6, respectively.

2. Study Area

The study area includes the beach of Serapo, located in the Central Thyrrenian Sea (Italy), which exhibits a rather regular morphology and rectilinear shoreline that is complexly long, approximately 1.45 km (Figure 1), aligned in the NW-SE direction (for the statistical processing, we considered only a 1.34 km-long shoreline, directly sampled with GPS). This beach is characterized by homogeneous grain size features with median diameter around 0.38 mm, indicating medium sands [37]. The topographic survey data, acquired in September 2017, refer to coastline and to five beach profiles T1–T5 as reported in Table 1. Coastline investigations were conducted in September 2018 (for the location, see Figure 1). Based on the difference in beach width and berm height, the studied beach can be subdivided into the following two stretches: a western beach stretch including profiles T1 and T2, which is 45–60 m wide and characterized by lower berm height (1.10–1.30 m) and a mean emerged beach slope of 5.5%; an eastern beach stretch including profiles T3, T4, and T5, which is characterized by higher beach width of 74–87 m and higher berm height of 1.29–1.46 m, with a lower emerged beach slope of 1.48–3.94%. This different beach width was already explained by Di Luccio et al. [37] in terms of partial clockwise beach rotation around a central pivotal point.
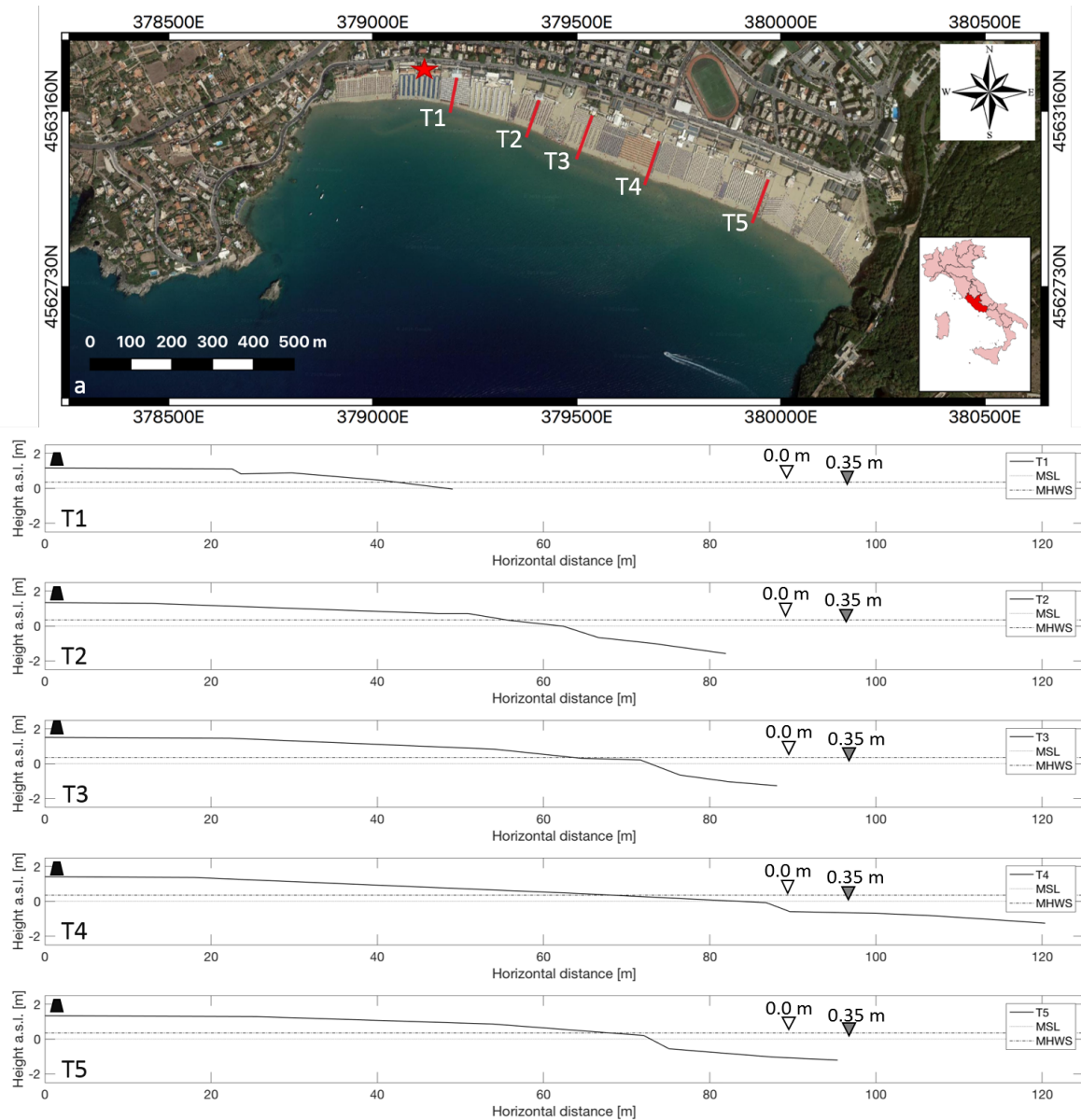
Figure 1. Serapo beach study area (**a**) with the location of the beach video camera system (red star) and the five investigated cross-shore transects (red lines), obtained by a beach survey conducted in September 2017; the beach profile along the transect with the location of the anthropic structures (black trapezium), Mean Sea Level (MSL), and the Mean Spring Tidal Range (MHSW), extracted by the official Italian tide archives (http://www.mareografico.it, last access: 30 April 2019) was reported for T1, T2, T3, T4, and T5. (basemap ©2018 Google product).

Table 1. Summary of Serapo beach's morphological characterization. The reported parameters are relative to the beach cross-shore profiles T1–T5.

Profile	Emerged Beach width L (m)	Berm Height (m)	Emerged Beach Slope β (%)	Local Beach Slope γ (%)
T1	45.38	1.11	7.88	5.85
T2	61.21	1.29	3.19	15.02
T3	73.54	1.46	3.94	17.27
T4	86.79	1.37	1.48	17.87
T5	74.02	1.29	3.88	21.37

3. Materials and Methods

3.1. Sea Waves' Analysis

The wave climate is connected to the methodology used for the definition of the coastline since the morphological changes affecting the beach after a sea storm can change the longitudinal beach profile (beach slope) in a more or less accentuated manner, influencing, as we shall see then, the remote acquisition processes. Moreover, if storm patterns and wave distributions (time scales) change, the coastline shape can evolve with erosion/accretion processes [38], inducing possible beach rotation, well evident with continuous video monitoring systems.

In order to define the sea condition characterizing the study area, we analyzed the historical time series extracted by the Ponza buoy 3-hourly data, provided by the Italian Sea Wave Measurement Network [39]. This directional pitch-roll buoy is moored in deep water [40], a few miles to the south of Ponza island (40°52′00.10″ N, 12°56′60.00″ E). The available parameters are significant wave height H_s, mean wave period T_m, and mean wave direction D_m, covering the years 1989–2014 (with some data gaps). Climatological wave analysis is presented, highlighting the wave storms that exposed a lower limit threshold of H_s equal to 2 m.

3.2. Kinematic GPS Survey

The Global Positioning System (GPS) surveying was employed to get the reference shoreline position. The collection of shore-parallel GPS positions was carried out in September 2017 using a single-frequency code and carrier phase receiver (Trimble Pathfinder ProXH) as the rover. The most common shoreline detection technique applied to visibly-discernible shoreline features is manual visual interpretation in the field, as reported by Boak and Turner [5]. In this paper, the shoreline was compiled by interpolating between described shore-normal beach profiles and a series of points collected along the beach face, which included maximum run-up limit and 0.5-m depth.

In order to compute the positioning solutions by various modes including single-point and relative positioning, post-processing of the raw data was performed using the RTKLIB software [41], an open-source software for standard and precise positioning [41]. The processing option for the relative positioning mode was set to carrier-based kinematic positioning; the ambiguity resolution was performed both recalculating the phase bias estimates every epoch (instantaneous) and using the Kalman filter to estimate the phase biases over many epochs (continuous). The last solution was much less noisy, as expected, and was adopted as the reference line. The analysis of the single point and carrier-based instantaneous solutions was included as well. In particular, the use of the single-point positioning was investigated as having the potential for being a low-cost method for shoreline mapping. In order to improve the results obtainable with this technique, the researchers have directed their studies towards the identification and reduction of multipath [42–44] as it is the highest source of error in the single-point positioning. In the last few months, smart phones equipped with a dual frequency multi-constellation GNSS receiver have appeared on the market. They could represent a valid and low-cost alternative to carry out the survey as shown by Robustelli et al. [45]. The position accuracy was evaluated on the basis of the calculation of the distance and azimuth of the estimated horizontal position error vector (Figure 2).
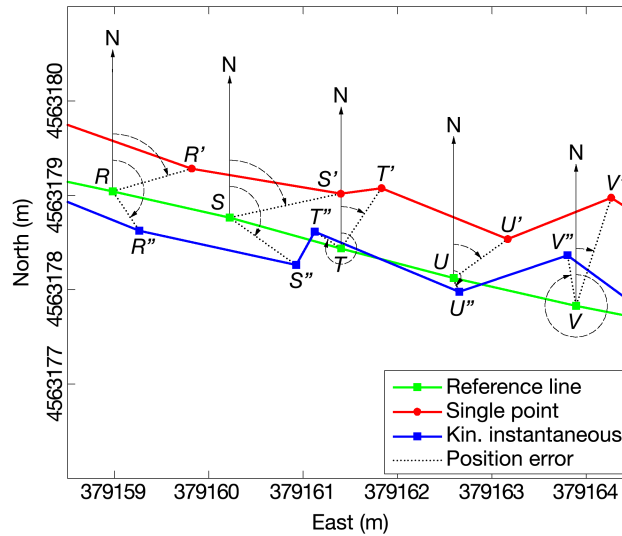
Figure 2. Scheme of the quantification of errors in the kinematic GPS horizontal positions referred to a portion of the trajectory.

Further analysis was carried out to discern also the effect of random GPS errors on the trajectory of the kinematic path. The magnitude of the effect due to random errors was identified through the computation of the deflection angle given by the angle between a V'W' line and the prolongation of the preceding U'V' line (Figure 3). Deflection angles were computed as positive or negative values depending on whether the line lied to the right (clockwise) or left (counterclockwise) of the prolongation of the preceding line.
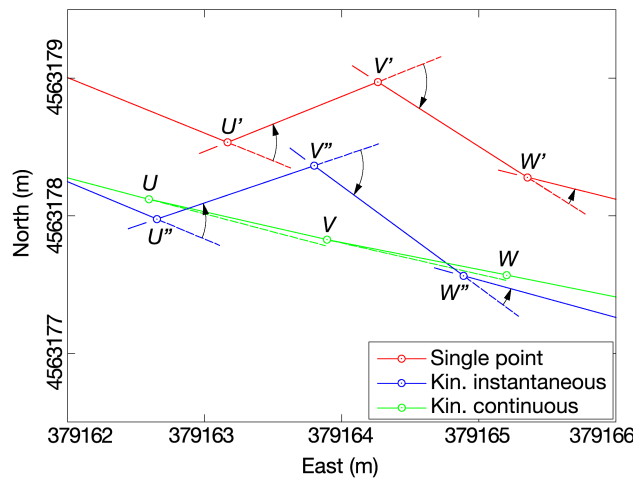

Figure 3. Scheme of the deflection angles referred to a portion of the trajectory.

3.3. Video Camera Observations

A video monitoring system was installed in the western part of Serapo beach (41°12′41.81″ N–13°33′29.66″ E) as shown in Figure 4. Two cameras provided a total view of the bay with 1920 ×1080 pixel resolution from an elevation of about 11 m above Mean Sea Level (MSL) and 100 m from the coastline. The mean pixel resolution was evaluated using the methodology suggested in Holland et al. [46]. Images were collected every second from 08:00 until 16:00 local time on a local video-recorder with a 2-TB storage capability from May 2017–June 2018. Optical measurements are subject to image distortions due to inherent camera characteristics [47]. According to Stumpf et al. [48] and Mucerino et al. [29], the images were calibrated using Ground Control Points (GCPs), which were placed in the view area of the cameras and were acquired in UTM-WGS84 using DGPS. The calibration process required at least nine GCPs for each camera that covered the entire camera view; camera system

calibration was performed by using 32 GCPs: 21 on the southeast side camera and 11 on west side camera. Finally, the image dataset was processed using Beachkeeper plus software [15].

Shoreline detection from the image was based on the physical consideration that the color contrast between beach and water is sufficient, lighting is strong enough, and the number of pixels in the water and beach groups is sufficient. Following Almar et al. [36] and other less recent authors [49–52], in order to reduce errors due to sea level variations, the shoreline was detected using the swash signature on timex average images, using images averaged over short periods (30 s), which significantly improved the accuracy of shoreline determination. The shoreline thus identified on the oblique image was converted to real-world coordinates using ortho-rectification techniques. Finally, shorelines obtained from corresponding images from the two cameras were managed to form a whole continuous shoreline.
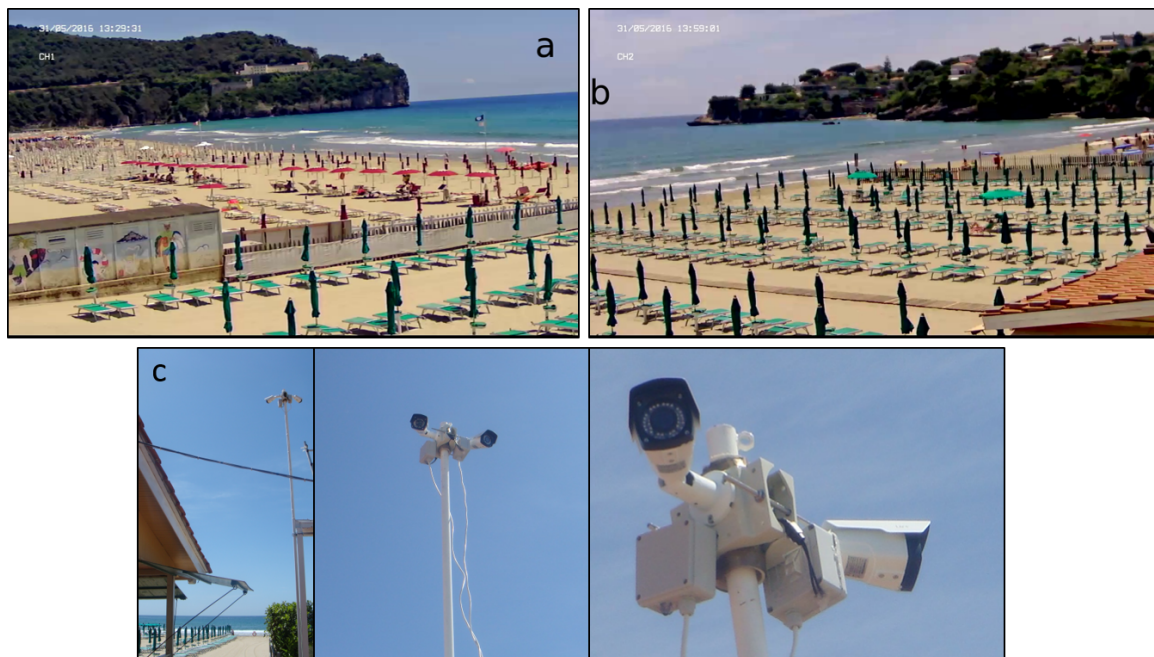

Figure 4. Camera system located on Serapo beach: (**a**) camera records, southeast side of the bay; (**b**) camera detections, west side of Serapo shoreline; (**c**) a detail of the camera installation.

3.4. Validation Method

The comparison between video and DGPS coastline has been performed on the whole beach, measuring the error as the deviation from the continuous DGPS line computed, depicted in green, along the normal to the DGPS itself for a sample of about 500 points. These points were chosen keeping constant the mutual distance (about 2.7 m) along the track.

In this paper, an error model for video camera measurements is proposed. The displacement offset with respect to the normal direction to the coastline can be computed by an exact trigonometric relation. In Figure 5, let ε_N represent the error in the normal direction to the coastline, ε_L the longitudinal error along the line of sight from the camera to the object, and ε_T the transverse error, perpendicular to the line of sight. The angle α is the angle between the coastline and the line of sight. If α has been observed, then:

$$\varepsilon_N = \varepsilon_L \sin\alpha + \varepsilon_T \cos\alpha \tag{1}$$
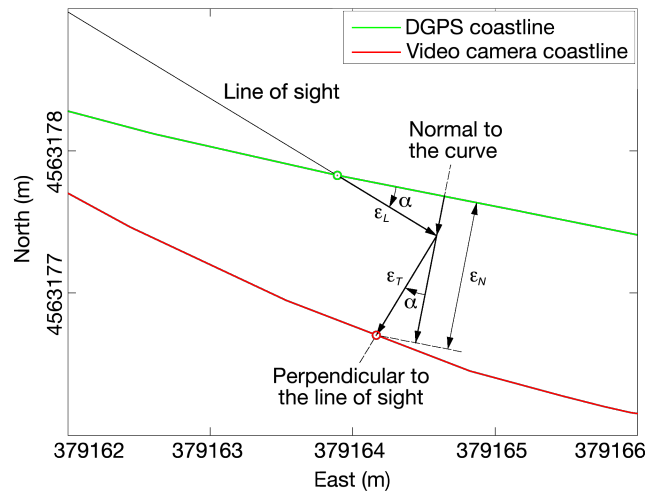
Figure 5. Scheme of the longitudinal and transverse error projections along the normal direction to the coastline.

The error model was based on two error components, the longitudinal ε_L and the transverse ε_T error, which were projected in the direction of the coastline's normal. The longitudinal and transverse errors were computed from the following equation:

$$\varepsilon_L = \varepsilon_T = aD - be^{cs} \tag{2}$$

where D is the distance of the shoreline from the video camera, s is the intertidal beach slope, e is Napier's constant, and a, b, c are three constants to be determined experimentally. In Equation (2), the correction be^{cs} may be applied to the distance-dependent error aD as the intertidal beach slope increases, which is in agreement with the inverse proportionality of the normal error with the beach slope [36].

Substituting Equation (2) into Equation 1 and if the longitudinal and transverse errors are grouped, this yields:

$$\varepsilon_N = \left(aD - be^{cs}\right)\left(\sin\alpha + \cos\alpha\right) \tag{3}$$

4. Results

4.1. Wave Climate Conditions

Significant wave height H_s, mean wave period T_m, and mean wave direction D_m, covering the years 1989–2014 (with some data gaps) are reported in Figure 6a–c, respectively. Maximum values of H_s for the ten highest wave storms recorded in the observation period are reported in Table 2, together with the mean period T_m, peak period T_p, and mean direction D_m associated with the storm peak. The highest H_s value was observed in December 1999, in agreement with Piscopia [53]. The selection of the ten highest storms showed that the directions of the storm waves were confined between 238° N and 272° N. This result is consistent with the one obtained with the selection of all the storms ($H_s > 2$ m) highlighted in red in Figure 6, showing that the highest waves were associated with southwestern, western, and northwestern directions [37]. With regard to astronomical sea level variations, the study area experiences a typical semi-diurnal tide, with a mean tidal range of 0.35 m, following the official Italian tide archives (http://www.mareografico.it, last access: 30 April 2019). However, main sea level variations due to meteorological surges can reach values up to 1 m [54].
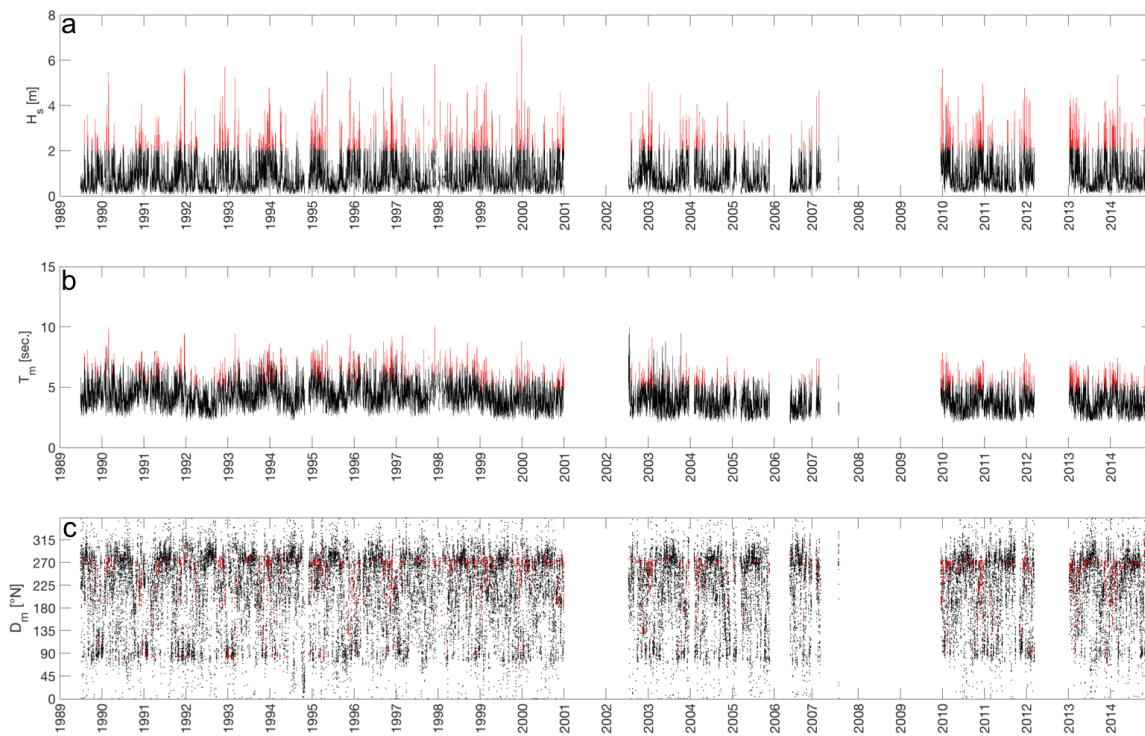
Figure 6. Offshore wave parameters (H_s in (**a**), T_m in (**b**), and D_m in (**c**)) recorded by the Ponza buoy during the years 1989–2014 with three-hourly time steps. The red color highlights the wave parameters associated with the highest waves ($H_s > 2$ m).

Table 2. Summary of the ten highest wave storm events recorded by the Ponza buoy in the period 1989–2014.

Storm Id	H_s max (m)	T_m (s)	T_p (s)	D_m (°N)	Date and Hour (UTC)
1	7.10	8.7	12.5	266.0	28 December 1999 15:00
2	5.80	10.0	11.1	272.0	3 December 1997 15:00
3	5.70	10.5	12.5	271.0	28 February. 1990 03:00
4	5.70	7.5	10.0	262.0	6 December 1992 03:00
5	5.61	7.9	10.5	264.6	2 January 2010 06:00
6	5.60	9.4	11.1	272.0	20 December 1991 15:00
7	5.50	8.9	10.0	266.0	13 May 1995 21:00
8	5.50	8.7	10.0	275.0	21 November 1996 06:00
9	5.50	7.7	10.0	238.0	19 November 1999 09:00
10	5.35	7.4	8.7	256.8	4 March 2014 06:00

4.2. Comparison between Different Accuracies of GPS Solutions

The results of the comparison of the single point and kinematic instantaneous GPS solutions with the continuous one are shown below.

As shown in Figure 7, the errors of the horizontal positions obtained in single-point mode reached a maximum value of 2.45 m, with a mean horizontal error of 0.93 m (Figure 7a). It should be noted that this average value was greater than the average error of the kinematic instantaneous solutions (Figure 7b) equal to 0.49 m. The standard deviation of the single point position errors was, however, comparable to that of the kinematic case, with a value of 0.28 m. Figure 7a also denotes a clear systematic error in terms of direction with prevailing azimuths towards northeast.
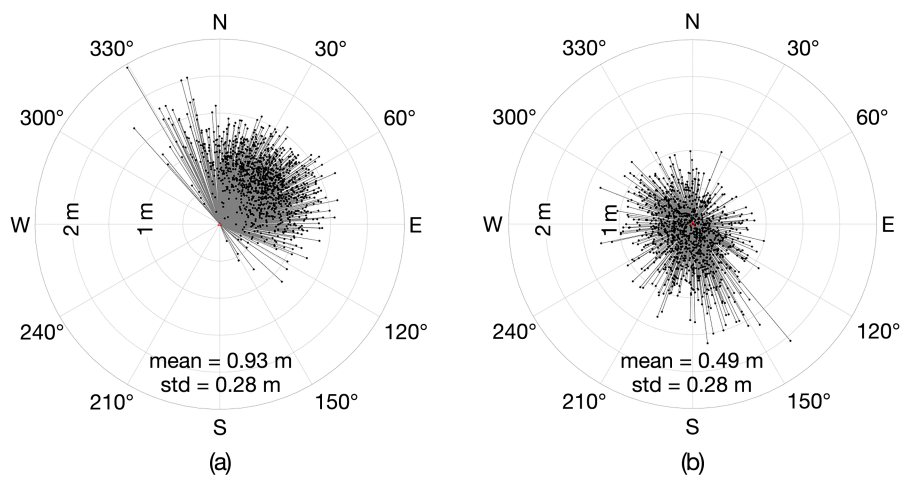
Figure 7. Single-point (**a**) and kinematic instantaneous (**b**) horizontal position error.

From the polar histogram of the azimuths shown in Figure 8, it is noted that about 85% of the single point error directions fell in the first quadrant from 0–90 degrees, with about 65% of the directions concentrated between the azimuth of 15 degrees and the azimuth of 75 degrees. This systematic error was reduced for the directions of the kinematic instantaneous errors; in fact, 85% of the errors were distributed in a range of greater amplitude, which extended from 0–240 degrees.
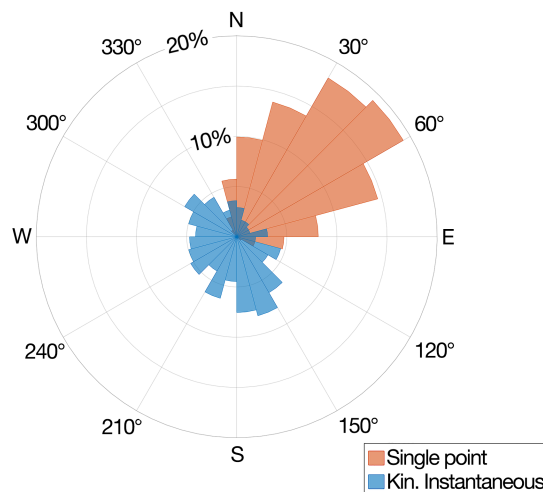

Figure 8. Histogram of the single-point and kinematic instantaneous error position azimuths.

With regard to the deflection angle analysis reported in the Methods, we computed its standard deviation, which was much lower for the kinematic continuous trajectory with respect to the single point and kinematic instantaneous ones, as reported in Figure 9. This circumstance confirms the capability of the kinematic continuous option for smoothing GPS data due to the use of Kalman filter.
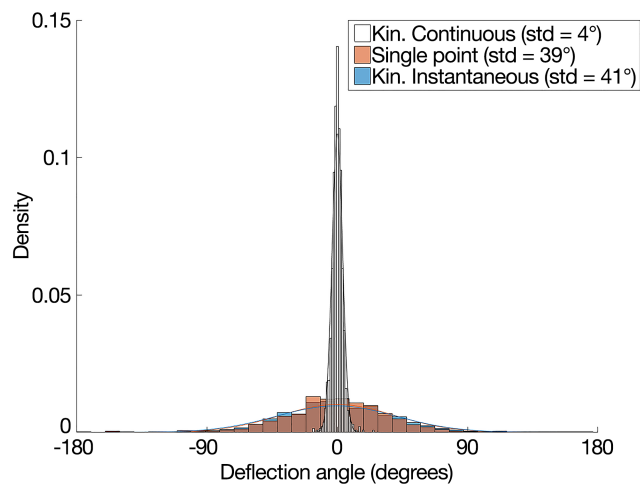
Figure 9. Histogram of the deflection angles.

4.3. Comparison between DGPS and Video Camera Coastline

In Figure 10, the comparison between the video camera coastline (in green) and the DGPS one (in red) is reported for four adjacent west-east beach sectors. The error distribution is not only dependent on the camera distance, as explained in the following.
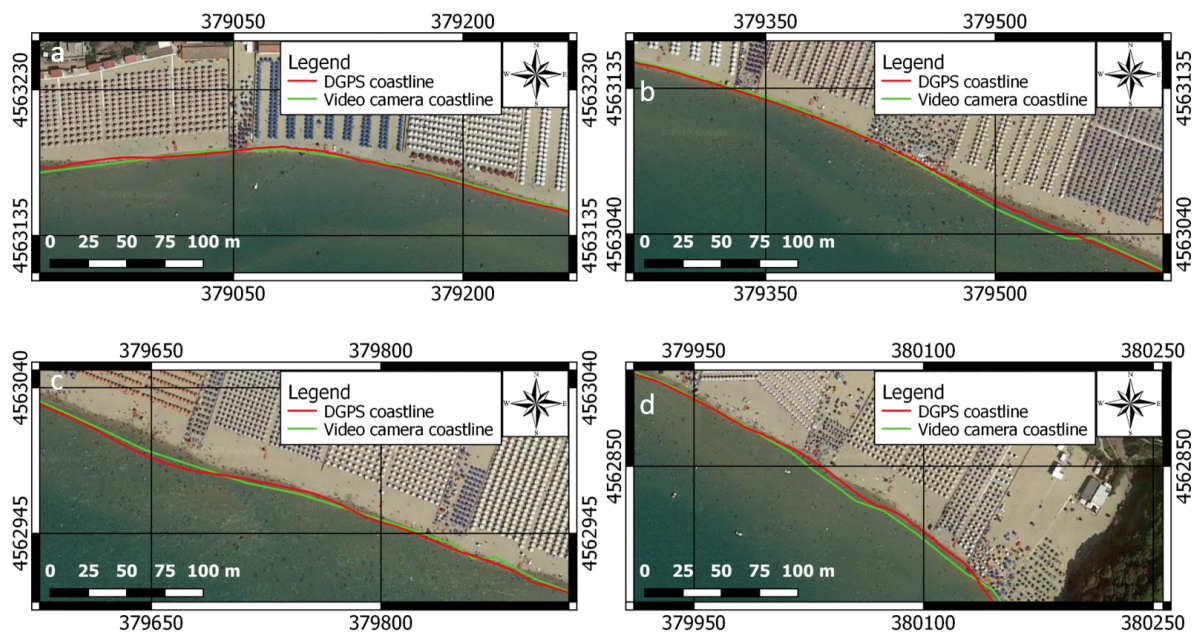

Figure 10. Video camera coastline (in green) compared with the DGPS coastline (in red) along Serapo beach. (basemap ©2018 Google product). In order to guarantee a better representation of the two coastlines, the beach has been divided into four sections, shown in the panels **a**–**d**, starting from west (panel **a**) to east (panel **d**).

In Figure 11a, we report in the chromatic scale the deviation between the two coastlines along the beach. Moreover, in Figure 11b, we report the error magnitude, neglecting the sign, as a function of the shoreline length. The following results can be synthesized.

First, the error exhibited a different amount between points located at a distance lower or higher than approximately one third of the beach extent, as shown from Figure 11b. In particular, for the eastern camera images, from the shoreline length of 200 m to a distance of 500 m, the error was around 1 m, while for the more distant points, the error was higher, with a maximum value of 5 m.
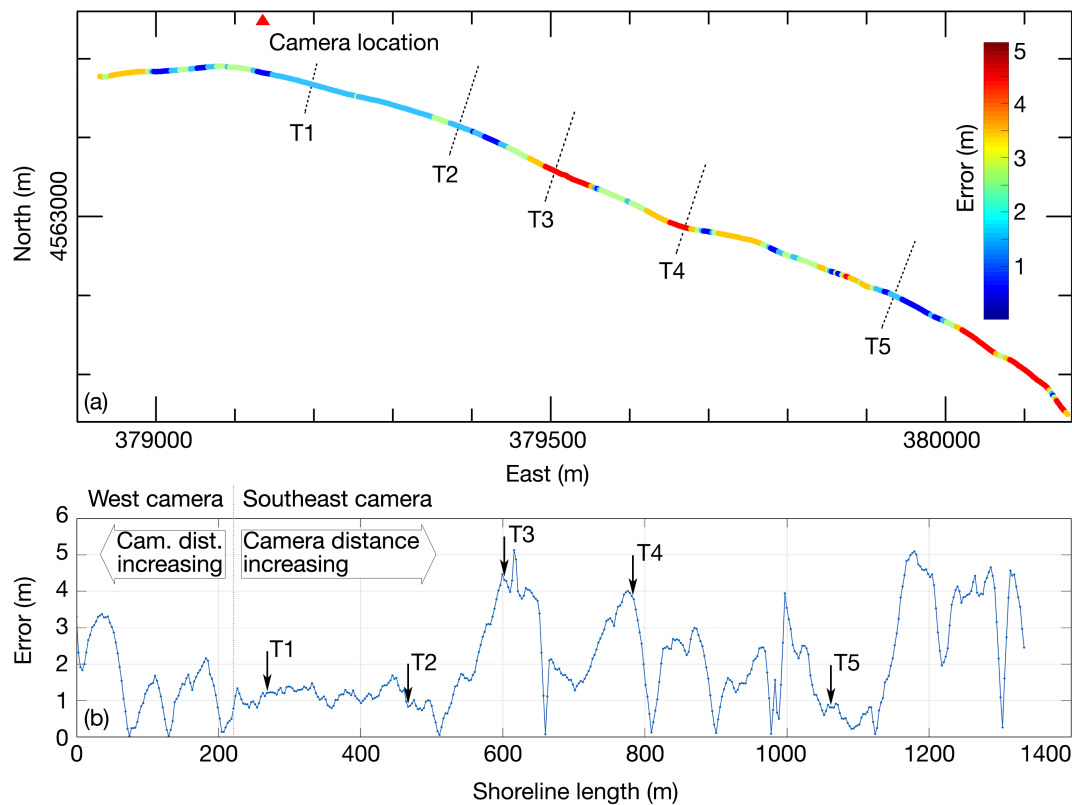
Figure 11. Observed deviations of the video coastline in the normal direction to the DGPS line for about 500 sample points. Panel a shows the deviations in the chromatic scale, in panel b the deviations are reported as function of the shoreline length.

Secondly, the error showed a lower standard deviation for the closer points; this is evident from the quite uniform color in Figure 11a if compared with the color variation along the second part of the coastline. The summary of the error statistics is reported in Table 3.

Table 3. Summary of the error statistics.

Distance (m)	Mean (m)	Max (m)	std (m)
0–200	1.62	3.37	0.97
200–500	1.08	1.69	0.29
500–1340	2.40	5.13	1.34

The inspection of the deviations between the remotely-measured coastline and the direct DGPS ones showed a lower error amount for points located at a distance closer than one third of the beach extent. This result has been obtained both in terms of maximum error (less than 2.0 m) and for the error standard deviation (less than 0.3 m). On the contrary, the more distant points exhibited a maximum error up to 5.0 m and an error standard deviation up to 1.3 m.

5. Discussion

In this paper, a shoreline detection technique from a low-cost video monitoring station was used, applying an automatic extraction technique that undertakes a water/beach distinction from color band ratios and a shoreline slope recognition module.

Prior to the validation of the video-derived shoreline with the direct survey, the differences between the single point and the unfiltered kinematic GPS have been examined. The results showed that the unfiltered kinematic GPS positions exhibited a better performance of the single-point GPS with

respect to the systematic error. Nevertheless, the latter presented a comparable standard deviation and a reduced cost both in terms of instruments and operational speed.

Compared to a direct DGPS survey, the video-derived coastline acquisition was less time consuming and more cost effective. The possibility to acquire a beach topography with a high temporal frequency can potentially highlight coastal processes during the winter season, when a direct survey is difficult due to harsh weather conditions.

To perform the error analysis, as stated previously (Equation (3)), it is useful to break the normal error into a distance-dependent part ε'_N and a slope-dependent one ε''_N.

The distance-dependent part can be estimated as:

$$\varepsilon'_N = aD\left(\sin\alpha + \cos\alpha\right) \tag{4}$$

where the constant a is computed experimentally from the field data; the values were 0.0125 and 0.0079 for the west side camera (from 0–200 m) and the southeast side camera (from 200–1340 m), respectively. Thus, the distance-dependent error is represented in Figure 12, with positive (negative) values indicating seaward (landward) offsets of the shoreline. The light blue curve represents normal errors that increase with the distance compared to the observed values (red curve). Figure 12 shows results obtained when the model is not corrected for the beach slope.
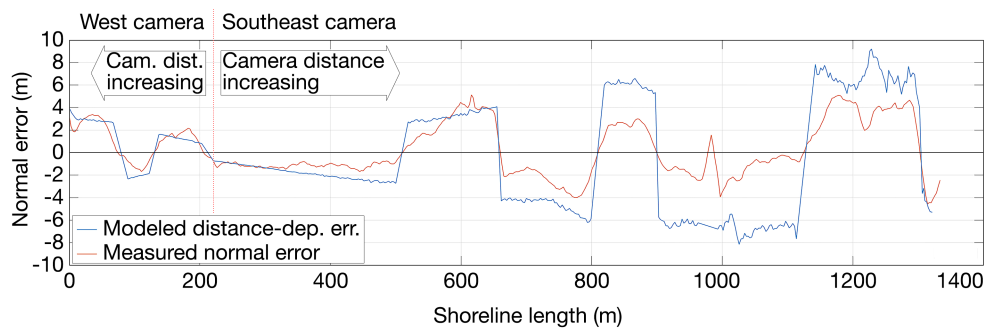

Figure 12. Distance-dependent part of the normal error.

In performing normal error estimation, it should be assumed that there are possible corrections due to the increasing intertidal beach slope. The model adopted to estimate these corrections is:

$$\varepsilon''_N = be^{cs}\left(\sin\alpha + \cos\alpha\right) \tag{5}$$

where the constants b and c are computed experimentally from the field data and the slope s is expressed in percent units. The constants b, c and the slope correction ε''_N have been calculated only for the stretch of coast between Transect 1 and Transect 5 for which the slope values have been obtained by interpolation. The values were 0.005 and 1/3 for the constants b and c, respectively. Figure 13 shows the relationship between the slope and the correction due to the beach slope.

Substituting the appropriate values into Equation (3), yields:

$$\varepsilon_N = \left(0.0079D - 0.005e^{\frac{s}{3}}\right)\left(\sin\alpha + \cos\alpha\right) \tag{6}$$

The result depends on the combination of three components including camera distance D, beach slope s, and the angle α between the coastline and the line of sight. The error model for video camera measurements has been tested to the extent between Transect 1 and Transect 5 due to the field data not enabling calculation of the beach slope and determining the error offset for the entire study area. Figure 14 shows the estimated normal errors determined by the final computed Equation (6). The particular combination produced results corresponding to those observed with the exception of the value at the shoreline length of 600 m.
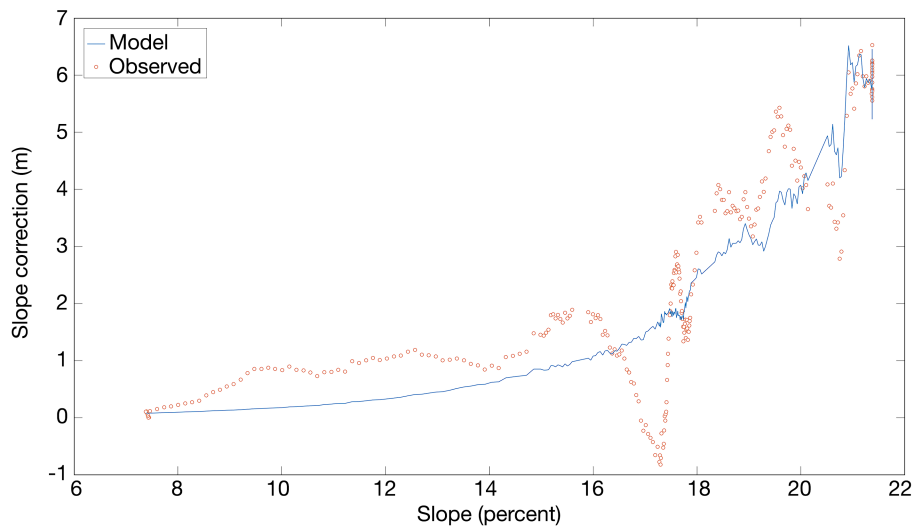
Figure 13. Slope correction due to the increasing intertidal beach slope between Transects 1 and 5.
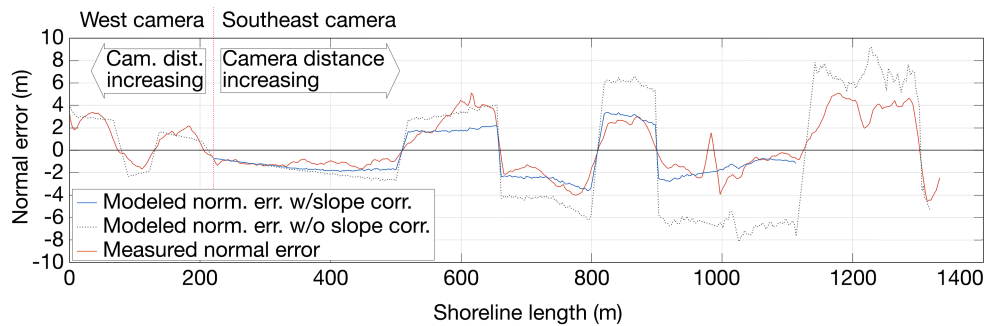

Figure 14. Estimated normal errors.

6. Conclusions

Currently, risk assessment plays a fundamental role in preventing irreversible erosion processes, as well as flooding damages. In this context, video monitoring represents a low-cost instrument to store a large amount of data with a high temporal frequency irrespective of weather conditions.

In this paper, we analyzed the limitations of the video-based coastline in terms of distance from the point of view and influence of beach topography. A shoreline detection technique from a low-cost video monitoring station was validated against DGPS-derived shoreline.

We introduced an error model, based on the transverse and longitudinal error along the line of sight, and computed a correction factor that can be applied to the distance-dependent error.

Wave storms alter the amounts of wave energy approaching a shore and can change the beach cross-shore profile, influencing the applicability of video monitoring acquisition systems.

Several types of coastal information can be provided from images. In Di Luccio et al. [16], we analyzed wave run-up; in the near future, we will use data for rip-current detection, which we already analyzed with direct and remote observation tools [14].

Day-light limitations of the video-derived data can be overcome by thermal cameras, which can operate also during night hours in order to monitor the beach during severe events. This goal will be the continuation of the present research, together with the challenge of modeling new algorithms to lower the deviation from direct measurements.

Author Contributions: Conceptualization G.P., G.B., U.R., D.D.L., L.M. Supervision G.B. Methodology G.P., G.B., U.R., D.D.L., L.M. Formal Analysis G.P., U.R., D.D.L. Validation G.P., G.B., U.R., D.D.L. Visualization G.P. and D.D.L. Software R.M. Data Curation R.M. Investigation, L.M. Writing—Original Draft Preparation G.P., U.R. and D.D.L. Writing—Review and Editing G.P., U.R. and D.D.L.

References

1. De Girolamo, P.; Di Risio, M.; Romano, A.; Molfetta, M. Landslide tsunami: Physical modeling for the implementation of tsunami early warning systems in the Mediterranean Sea. *Procedia Eng.* **2014**, *70*, 429–438. [CrossRef]

2. Samaras, A.; Karambas, T.V.; Archetti, R. Simulation of tsunami generation, propagation and coastal inundation in the Eastern Mediterranean. *Ocean Sci.* **2015**, *11*, 643–655. [CrossRef]

3. Small, C.; Nicholls, R.J. A global analysis of human settlement in coastal zones. *J. Coast. Res.* **2003**, *19*, 584–599.

4. Di Risio, M.; Bruschi, A.; Lisi, I.; Pesarino, V.; Pasquali, D. Comparative analysis of coastal flooding vulnerability and hazard assessment at national scale. *J. Mar. Sci. Eng.* **2017**, *5*, 51. [CrossRef]

5. Boak, E.H.; Turner, I.L. Shoreline definition and detection: A review. *J. Coast. Res.* **2005**, *21*, 688–703. [CrossRef]

6. Bruno, M.F.; Molfetta, M.G.; Pratola, L.; Mossa, M.; Nutricato, R.; Morea, A.; Nitti, D.O.; Chiaradia, M.T. A Combined Approach of Field Data and Earth Observation for Coastal Risk Assessment. *Sensors* **2019**, *19*, 1399. [CrossRef] [PubMed]

7. Bruno, M.F.; Molfetta, M.G.; Mossa, M.; Morea, A.; Chiaradia, M.T.; Nutricato, R.; Nitti, D.O.; Guerriero, L.; Coletta, A. Integration of multitemporal SAR/InSAR techniques and NWM for coastal structures monitoring: Outline of the software system and of an operational service with COSMO-SkyMed data. In Proceedings of the 2016 IEEE Workshop on Environmental, Energy, and Structural Monitoring Systems (EESMS), Bari, Italy, 13–14 June 2016; pp. 1–6.

8. Holman, R.A.; Stanley, J. The history and technical capabilities of Argus. *Coast. Eng.* **2007**, *54*, 477–491. [CrossRef]

9. Valentini, N.; Saponieri, A.; Molfetta, M.G.; Damiani, L. New algorithms for shoreline monitoring from coastal video systems. *Earth Sci. Inform.* **2017**, *10*, 495–506. [CrossRef]

10. Benassai, G.; Di Luccio, D.; Mucerino, L.; Paola, G.D.; Rosskopf, C.M.; Pugliano, G.; Robustelli, U.; Montella, R. Shoreline rotation analysis of embayed beaches in the Central Thyrrenian Sea. In Proceedings of the 2018 IEEE International Workshop on Metrology for the Sea; Learning to Measure Sea Health Parameters (MetroSea), Bari, Italy, 8–10 October 2018; pp. 7–12. [CrossRef]

11. Guariglia, A.; Buonamassa, A.; Losurdo, A.; Saladino, R.; Trivigno, M.L.; Zaccagnino, A.; Colangelo, A. A multisource approach for coastline mapping and identification of shoreline changes. *Ann. Geophys.* **2006**, *49*, 295–304.

12. Alesheikh, A.A.; Ghorbanali, A.; Nouri, N. Coastline change detection using remote sensing. *Int. J. Environ. Sci. Technol.* **2007**, *4*, 61–66. [CrossRef]

13. Nunziata, F.; Buono, A.; Migliaccio, M.; Benassai, G. Dual-polarimetric C-and X-band SAR data for coastline extraction. *IEEE J. Sel. Top. Appl. Earth Obs. Remote Sens.* **2016**, *9*, 4921–4928. [CrossRef]

14. Benassai, G.; Aucelli, P.; Budillon, G.; De Stefano, M.; Di Luccio, D.; Di Paola, G.; Montella, R.; Mucerino, L.; Sica, M.; Pennetta, M. Rip current evidence by hydrodynamic simulations, bathymetric surveys and UAV observation. *Nat. Hazards Earth Syst. Sci.* **2017**, *17*, 1493–1503. [CrossRef]

15. Brignone, M.; Schiaffino, C.F.; Isla, F.I.; Ferrari, M. A system for beach video-monitoring: Beachkeeper plus. *Comput. Geosci.* **2012**, *49*, 53–61. [CrossRef]

16. Di Luccio, D.; Benassai, G.; Budillon, G.; Mucerino, L.; Montella, R.; Pugliese Carratelli, E. Wave run-up prediction and observation in a micro-tidal beach. *Nat. Hazards Earth Syst. Sci.* **2018**, *18*, 2841–2857. [CrossRef]

17. Aarninkhof, S.G.J. Nearshore Bathymetry Derived From Video Imagery. Ph.D. Thesis, Delft University of Technology, Delft, The Netherlands, 2003.

18. Turner, I.L.; Aarninkhof, S.; Dronkers, T.; McGrath, J. CZM applications of Argus coastal imaging at the Gold Coast, Australia. *J. Coast. Res.* **2004**, *20*, 739–752. [CrossRef]

19. Montuori, A.; Ricchi, A.; Benassai, G.; Migliaccio, M. Sea wave numerical simulation and verification in Tyrrhenian costal area with X-band cosmo-skymed SAR data. In Proceedings of the ESA, SOLAS & EGU Joint Conference Earth Observation for Ocean-Atmosphere Interactions Science, Frascati, Italy, 29 November–2 December 2011; Volume 29.

20. Benassai, G.; Montuori, A.; Migliaccio, M.; Nunziata, F. Sea wave modeling with X-band COSMO-SkyMed© SAR-derived wind field forcing and applications in coastal vulnerability assessment. *Ocean Sci.* **2013**, *9*, 325–341. [CrossRef]

21. Benassai, G.; Migliaccio, M.; Montuori, A.; Ricchi, A. Wave simulations through SAR COSMO-SkyMed wind retrieval and verification with buoy data. In Proceedings of the Twenty-second International Offshore and Polar Engineering Conference. International Society of Offshore and Polar Engineers, Rhodes, Greece, 17–22 June 2012.

22. Dominici, D.; Zollini, S.; Alicandro, M.; Della Torre, F.; Buscema, P.M.; Baiocchi, V. High Resolution Satellite Images for Instantaneous Shoreline Extraction Using New Enhancement Algorithms. *Geosciences* **2019**, *9*, 123. [CrossRef]

23. Palazzo, F.; Latini, D.; Baiocchi, V.; Del Frate, F.; Giannone, F.; Dominici, D.; Remondiere, S. An application of COSMO-Sky Med to coastal erosion studies. *Eur. J. Remote Sens.* **2012**, *45*, 361–370. [CrossRef]

24. Benassai, G.; Di Luccio, D.; Corcione, V.; Nunziata, F.; Migliaccio, M. Marine Spatial Planning Using High-Resolution Synthetic Aperture Radar Measurements. *IEEE J. Ocean. Eng.* **2018**, *43*, 586–594. [CrossRef]

25. Di Tullio, G.R.; Mariani, P.; Benassai, G.; Di Luccio, D.; Grieco, L. Sustainable use of marine resources through offshore wind and mussel farm co-location. *Ecol. Model.* **2018**, *367*, 34–41. [CrossRef]

26. Benassai, G.; Di Luccio, D.; Migliaccio, M.; Cordone, V.; Budillon, G.; Montella, R. High resolution remote sensing data for environmental modeling: Some case studies. In Proceedings of the 2017 IEEE 3rd International Forum on Research and Technologies for Society and Industry (RTSI), Modena, Italy, 11–13 September 2017; pp. 1–5.

27. Nunziata, F.; Buono, A.; Migliaccio, M.; Benassai, G.; Di Luccio, D. Shoreline erosion of microtidal beaches examined with UAV and remote sensing techniques. In Proceedings of the 2018 IEEE International Workshop on Metrology for the Sea; Learning to Measure Sea Health Parameters (MetroSea), Bari, Italy, 8–10 October 2018; pp. 162–166. [CrossRef]

28. Di Luccio, D.; Benassai, G.; Di Paola, G.; Rosskopf, C.; Mucerino, L.; Montella, R.; Contestabile, P. Monitoring and modeling coastal vulnerability and mitigation proposal for an archaeological site (Kaulonia, Southern Italy). *Sustainability* **2018**, *10*, 2017. [CrossRef]

29. Mucerino, L.; Albarella, M.; Carpi, L.; Besio, G.; Benedetti, A.; Corradi, N.; Firpo, M.; Ferrari, M. Coastal exposure assessment on Bonassola bay. *Ocean Coast. Manag.* **2019**, *167*, 20–31. [CrossRef]

30. Schiaffino, C.F.; Dessy, C.; Corradi, N.; Fierro, G.; Ferrari, M. Morphodynamics of a gravel beach protected by a detached low-crested breakwater. The case of Levanto (eastern Ligurian Sea, Italy). *Ital. J. Eng. Geol. Environ.* **2015**, *15*, 31–39.

31. Lisi, I.; Molfetta, M.; Bruno, M.; Di Risio, M.; Damiani, L. Morphodynamic classification of sandy beaches in enclosed basins: The case study of Alimini (Italy). *J. Coast. Res.* **2011**, 180–184.

32. Postacchini, M.S.L.L.C.; Mancinelli, A. Medium-term dynamics of a middle Adriatic barred beach. *Ocean Sci.* **2017**, *3*, 719. [CrossRef]

33. Plant, N.G.; Holman, R.A. Intertidal beach profile estimation using video images. *Mar. Geol.* **1997**, *140*, 1–24. [CrossRef]

34. Bryan, K.R.; Smith, R.; Ovenden, R. The Use of a Video Camera to Assess Beach Volume Change During 2001 at Tairua, New Zealand. In *Coasts & Ports 2003 Australasian Conference, Proceedings of the 16th Australasian Coastal and Ocean Engineering Conference, the 9th Australasian Port and Harbour Conference and the Annual New Zealand Coastal Society Conference*; Institution of Engineers: Canberra, Australia, 2003; p. 1236.

35. Smith, R.; Bryan, K. Monitoring beach face volume with a combination of intermittent profiling and video imagery. *J. Coast. Res.* **2007**, *23*, 892–898. [CrossRef]

36. Almar, R.; Ranasinghe, R.; Sénéchal, N.; Bonneton, P.; Roelvink, D.; Bryan, K.R.; Marieu, V.; Parisot, J.P. Video-based detection of shorelines at complex meso–macro tidal beaches. *J. Coast. Res.* **2012**, *28*, 1040–1048.

37. Di Luccio, D.; Benassai, G.; Di Paola, G.; Mucerino, L.; Buono, A.; Rosskopf, C.M.; Nunziata, F.; Migliaccio, M.; Urciuoli, A.; Montella, R. Shoreline Rotation Analysis of Embayed Beaches by Means of In Situ and Remote Surveys. *Sustainability* **2019**, *11*, 725. [CrossRef]

38. Slott, J.M.; Murray, A.B.; Ashton, A.D.; Crowley, T.J. Coastline responses to changing storm patterns. *Geophys. Res. Lett.* **2006**, *33*. [CrossRef]

39. Bencivenga, M.; Nardone, G.; Ruggiero, F.; Calore, D. The Italian data buoy network (RON). *Adv. Fluid Mech. IX* **2012**, *74*, 321.

40. Arena, F.; Pavone, D. Return period of nonlinear high wave crests. *J. Geophys. Res. Ocean.* **2006**, *111*. [CrossRef]

41. Takasu, T. RTKLIB Ver. 2.4.2 Manual. Available online: http://www.rtklib.com/prog/manual_2.4.2.pdf (accessed on 23 November 2018).

42. Pugliano, G.; Robustelli, U.; Rossi, F.; Santamaria, R. A new method for specular and diffuse pseudorange multipath error extraction using wavelet analysis. *GPS Solut.* **2016**, *20*, 499–508. [CrossRef]

43. Robustelli, U.; Pugliano, G. GNSS code multipath short time fourier transform analysis. *Navi* **2018**, *65*, 353–362. [CrossRef]

44. Robustelli, U.; Pugliano, G. Code multipath analysis of Galileo FOC satellites by time-frequency representation. *Appl. Geomat.* **2018**, *11*, 69–80. [CrossRef]

45. Robustelli, U.; Baiocchi, V.; Pugliano, G. Assessment of Dual Frequency GNSS Observations from a Xiaomi Mi 8 Android Smartphone and Positioning Performance Analysis. *Electronics* **2019**, *8*, 91. [CrossRef]

46. Holland, K.T.; Holman, R.A.; Lippmann, T.C.; Stanley, J.; Plant, N. Practical use of video imagery in nearshore oceanographic field studies. *IEEE J. Ocean. Eng.* **1997**, *22*, 81–92. [CrossRef]

47. Didier, D.; Bernatchez, P.; Augereau, E.; Caulet, C.; Dumont, D.; Bismuth, E.; Cormier, L.; Floc'h, F.; Delacourt, C. LiDAR validation of a video-derived beachface topography on a tidal flat. *Remote Sens.* **2017**, *9*, 826. [CrossRef]

48. Stumpf, A.; Augereau, E.; Delacourt, C.; Bonnier, J. Photogrammetric discharge monitoring of small tropical mountain rivers: A case study at Rivière des Pluies, Réunion Island. *Water Resour. Res.* **2016**, *52*, 4550–4570. [CrossRef]

49. Aarninkhof, S. Argus-based monitoring of intertidal beach morphodynamics. In Proceedings of the Coastal Sediments 99, Long Island, NY, USA, 21–23 June 1999.

50. Alexander, P.S.; Holman, R.A. Quantification of nearshore morphology based on video imaging. *Mar. Geol.* **2004**, *208*, 101–111. [CrossRef]

51. Davidson, M.; Aarninkhof, S.; Van Koningsveld, M.; Holman, R. Developing coastal video monitoring systems in support of coastal zone management. *J. Coast. Res.* **2006**, *I*, 49–56.

52. Holman, R.; Stanley, J.; Ozkan-Haller, T. Applying video sensor networks to nearshore environment monitoring. *IEEE Pervasive Comput.* **2003**, *2*, 14–21. [CrossRef]

53. Piscopia, R.; Inghilesi, R.; Panizzo, A.; Corsini, S.; Franco, L. Analysis of 12-year wave measurements by the Italian Wave Network. In *Coastal Engineering 2002: Solving Coastal Conundrums*; World Scientific: Singapore, 2003; pp. 121–133.

54. Cazenave, A.; Bonnefond, P.; Mercier, F.; Dominh, K.; Toumazou, V. Sea level variations in the Mediterranean Sea and Black Sea from satellite altimetry and tide gauges. *Glob. Planet. Chang.* **2002**, *34*, 59–86. [CrossRef]